

# Intrinsic dissipation mechanisms in metallic glass resonators

Meng Fan,<sup>1,2</sup> Aya Nawano,<sup>1,2</sup> Jan Schroers,<sup>1,2</sup> Mark D. Shattuck,<sup>3,1</sup> and Corey S. O'Hern<sup>1,2,4,5</sup>

<sup>1</sup>*Department of Mechanical Engineering and Materials Science,  
Yale University, New Haven, Connecticut, 06520, USA*

<sup>2</sup>*Center for Research on Interface Structures and Phenomena,  
Yale University, New Haven, Connecticut, 06520, USA*

<sup>3</sup>*Department of Physics and Benjamin Levich Institute,  
The City College of the City University of New York, New York, New York, 10031, USA*

<sup>4</sup>*Department of Physics, Yale University, New Haven, Connecticut, 06520, USA*

<sup>5</sup>*Department of Applied Physics, Yale University, New Haven, Connecticut, 06520, USA*

Micro- and nano-resonators have important applications including sensing, navigation, and biochemical detection. Their performance is quantified using the quality factor  $Q$ , which gives the ratio of the energy stored to the energy dissipated per cycle. Metallic glasses are a promising materials class for micro- and nano-scale resonators since they are amorphous and can be fabricated precisely into complex shapes on these lengthscales. To understand the intrinsic dissipation mechanisms that ultimately limit large  $Q$ -values in metallic glasses, we perform molecular dynamics simulations to model metallic glass resonators subjected to bending vibrations. We calculate the vibrational density of states, redistribution of energy from the fundamental mode of vibration, and  $Q$  versus the kinetic energy per atom  $K$  of the excitation. In the linear and nonlinear response regimes where there are no atomic rearrangements, we find that  $Q \rightarrow \infty$  (since we do not consider coupling to the environment). We identify a characteristic  $K_r$  above which atomic rearrangements occur, and there is significant energy leakage from the fundamental mode to higher frequencies, causing finite  $Q$ . Thus,  $K_r$  is a critical parameter determining resonator performance. We show that  $K_r$  decreases as a power-law,  $K_r \sim N^{-k}$ , with increasing system size  $N$ , where  $k \approx 1.3$ . We estimate the critical strain  $\langle \gamma_r \rangle \sim 10^{-8}$  for micron-sized resonators below which atomic rearrangements do not occur, and thus large  $Q$ -values can be obtained when they are operated below  $\gamma_r$ . We find that  $K_r$  for amorphous resonators is comparable to that for resonators with crystalline order.

## I. INTRODUCTION

Micro- and nano-resonators have numerous important applications including navigation, sensing, chemical detection, molecular separation, and biological imaging [1]. The performance of resonators is typically measured by the quality factor,  $Q$ , which gives the ratio of the energy stored to the energy dissipated per cycle in the resonator during operation [2]. Micro- and nano-resonators made from non-metallic crystalline materials, such as sapphire [3], carbon nanotubes [4, 5], and single-crystal diamond [6] can possess quality factors  $Q > 10^6$  at low temperatures. However, it is difficult to fabricate these materials into complex shapes, and many applications require electrical conduction. As a result, crystalline metals are used in many resonator applications, yet these suffer from energy losses that arise from topological defects and grain boundaries [7].

In an effort to obviate energy losses from topological defects and grain boundaries that occur in crystalline metals, as well as take advantage of their plastic-forming ability to be fabricated into complex shapes, several groups have considered resonators made from metallic glasses (MGs) [8–12]. MGs are cooled rapidly to avoid crystallization, and thus they possess uniformly disordered structure. Recent experiments have shown that metallic-glass-based resonators can achieve quality factors that are comparable and even larger than those for resonators made from crystalline metals [9]. Metallic

glasses offer the additional benefit for resonator applications in that they can be thermoplastically formed into complex shapes with spatial features that span many orders of magnitude [13–15]. In this work, we seek to characterize the dissipation mechanisms that determine the quality factor for metallic glass resonators.

The mechanisms that give rise to energy losses during vibration can be classified as intrinsic or extrinsic [1]. Extrinsic losses, such as anchoring and frictional losses, come from interactions between the resonator and its surrounding environment [16, 17]. In contrast, intrinsic losses originate from flaws or defects within the resonator, such as dislocations, grain boundaries, vacancies, and interstitials in crystalline materials. In metallic glasses, which lack crystalline order, intrinsic losses are envisioned to stem from irreversible, collective atomic rearrangements, or shear-transformation zones (STZs) [18]. A number of studies have characterized the role of collective atomic rearrangements in determining the mechanical properties of metallic glasses, including ductility, yielding, and shear-band formation [19–23].

Internal friction measurements have been performed to gain insight into intrinsic dissipation mechanisms and the quality factor of metallic glasses [7, 24, 25]. However, a key focus in this work has been on revealing structural relaxation processes at elevated temperatures, rather than their room temperature behavior (which is typically significantly below the glass transition temperature). In these studies, metallic glass samples are typically perturbed by mechanical or electrostatic excitation using a

torsion pendulum or dynamical mechanical analyzer, and the internal friction is measured as a function of temperature, frequency, and strain amplitude [7, 26, 27]. The internal friction, which is proportional to  $Q^{-1}$ , is generally small for temperatures below room temperature, and then increases dramatically, forming a strong peak at temperatures typically above 400-500 K due to collective  $\alpha$  structural relaxations [8, 28, 29]. Studies [7] have also reported a much smaller peak (typically four orders of magnitude smaller than that corresponding to  $\alpha$  relaxations) in the internal friction of metallic glasses between 50 K and room temperature. Researchers have suggested that this peak corresponds to localized, anelastic so-called  $\beta$  relaxations. Explanations of the peaks in the internal friction include the creation and destruction of free volume [30], dislocation motion [31], shear transformation zones [18], shear bands, and other mechanisms that involve structural rearrangements. At even lower temperatures ( $< 50$  K), the internal friction has been described using the quantum mechanical tunneling model for two-level systems [32, 33].

Most of these prior studies of the vibrational properties of metallic glasses either use a quantum mechanical approach for the low-temperature behavior or consider temperatures near room temperature and above, where thermal fluctuations are significant and microscopic rearrangements of atoms are frequent. In this work, we will take a different, but still classical approach, and focus on the nearly zero-temperature regime, where even microscopic rearrangements of atoms are rare, to better understand the transition from the linear response regime where  $Q$  is infinite (since we do not consider coupling of the system to the environment) to the highly nonlinear regime where  $Q$  becomes finite.

We carry out molecular dynamics (MD) simulations to quantify the intrinsic dissipation caused by atomic rearrangements and measure the quality factor in model metallic glass resonators. We induce vibrations in a thin bar-shaped resonator by exciting the mode corresponding to the resonator's fundamental frequency with a given kinetic energy per atom  $K$  and then running MD at constant total energy. When  $K$  is small, i.e.  $K < K_{nl}$ , the resonator displays linear response, the spectrum of the vibrational modes only includes the fundamental mode, and  $Q \rightarrow \infty$ . For intermediate  $K$ , i.e.  $K_{nl} < K < K_r$ , energy leaks to modes other than the fundamental mode, but at sufficiently long times the leakage stops. Thus, in this regime,  $Q \rightarrow \infty$  at long times. For  $K > K_r$ , the system undergoes one or more atomic rearrangements, which induce strong dissipation and finite  $Q$ . Thus, the magnitude of  $K_r$  controls the performance of metallic glass resonators. We further show that  $K_r$  can be increased by decreasing the system size or by decreasing the cooling rate used to prepare the resonator. We also show that resonators with amorphous structure can achieve comparable performance (e.g. same  $Q$ ) to those with partial crystalline order.

The remainder of the article is organized as follows.

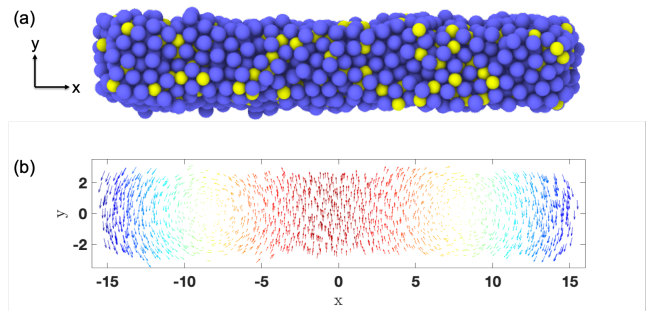


Figure 1: (a) View of the model metallic glass resonator along the  $z$  axis. The bar contains  $N = 2000$  atoms with aspect ratio  $L_x : L_y : L_z = 6 : 1 : 2$ . Blue and yellow atoms indicate  $A$  and  $B$  atom types, respectively. (b) Vector field representing the fundamental mode of the dynamical matrix of the metallic glass resonator in (a). The color scale highlights the  $y$ -component of the fundamental mode contribution for each atom with red corresponding to positive and blue corresponding to negative  $y$ -values.

In Sec. II, we describe the simulation methods we use to prepare and excite the metallic glass resonators, and to quantify the energy loss and quality factor of the vibrations. In Sec. III, we present the results, including measurements of the intrinsic loss and dissipation arising from nonlinearity and atomic rearrangements, techniques to increase  $Q$  by decreasing the system size and cooling rate, and comparisons of resonator performance in amorphous and crystalline samples. In Sec. IV, we summarize our findings and present promising directions for future research. We also include two Appendices. In Appendix A, we show that our results for the vibrational response do not depend strongly on the length of the time series of the vibrations that we collect. In Appendix B, we show the time dependence of the vibrational density of states, which supports the findings presented in the main text.

## II. MODELS AND METHODS

We perform molecular dynamics (MD) simulations of binary Lennard Jones mixtures using the Kob-Andersen model [34], which has been employed to describe NiP alloys. Spherical atoms interact pairwise via the shifted-force version of the Lennard-Jones potential,  $u(r_{ij}) = 4\epsilon_{ij}[(\sigma_{ij}/r_{ij})^{12} - (\sigma_{ij}/r_{ij})^6]$  with a cutoff distance  $r_c = 2.5\sigma_{ij}$ , where  $r_{ij}$  is the separation between atoms  $i$  and  $j$ . The total potential energy per atom is  $U = N^{-1} \sum_{i>j} u(r_{ij})$ . 80% of the atoms are type A ( $N_A/N = 0.8$ ) and 20% are type B ( $N_B/N = 0.2$ ), where  $N = N_A + N_B$  is the total number of atoms, and the energy and length parameters are given by  $\epsilon_{AA} = 1.0$ ,  $\epsilon_{BB} = 0.5$ ,  $\epsilon_{AB} = 1.5$ ,  $\sigma_{AA} = 1.0$ ,  $\sigma_{BB} = 0.88$ , and  $\sigma_{AB} = 0.8$ . All atoms have the same mass  $m$ . The energy, length, and pressure scales are given in terms of  $\epsilon_{AA}$ ,  $\sigma_{AA}$ , and  $\epsilon_{AA}/\sigma_{AA}^3$ , respectively.

We initially placed the  $N$  atoms on an FCC lattice in a long, thin box with aspect ratio  $L_x : L_y : L_z = 6 : 1 : 2$  and periodic boundaries in the  $x$ -,  $y$ -, and  $z$ -directions at reduced number density  $\rho = 1.0$ . We then equilibrated the system at high temperature  $T_0 > T_g \sim 0.4$  [35] (which melts the crystal) by running molecular dynamics simulations at fixed number of atoms, pressure, and temperature (NPT) using the Nosé-Hoover thermostat with temperature  $T_0 = 0.6$  and pressure  $P_0 = 0.025$ , a modified velocity-Verlet integration scheme, and time step  $\Delta t = 10^{-3}$ . We then cool the system into a glassy state at zero temperature using a linear cooling ramp with time  $\bar{t}$ , such that  $T(\bar{t}) = T_0 - R\bar{t}$ . (The cooling rate is measured in units of  $\epsilon_{AA}^{3/2}/(m^{1/2}\sigma_{AA})$ , where the Boltzmann constant  $k_B = 1$ .) We varied the cooling rate  $R$  over more than three orders of magnitude, yet we ensured that  $R$  was larger than the critical cooling rate  $R_c$  to avoid crystallization. We vary  $N$  from 250 to 8000 atoms to assess the finite size effects.

After cooling the system to zero temperature, we remove the periodic boundary conditions in the  $x$ -,  $y$ -, and  $z$ -directions (creating free surfaces) and then apply conjugate gradient energy minimization to yield the zero-temperature configuration of the resonator,  $\mathbf{R}_0 = \{x_1, y_1, z_1, \dots, x_N, y_N, z_N\}$ . (See Fig. 1 (a).) To induce vibrations, we excite the fundamental mode, i.e. the lowest eigenfrequency  $\omega_1$  of the dynamical matrix [36], evaluated at  $\mathbf{R}_0$ . (See Fig. 1 (b).) The elongated, thin shape of the resonator guarantees that the lowest eigenfrequency is well-separated from higher ones. We then set the initial velocities of the atoms, such that  $\mathbf{v} = \{v_{x1}, v_{y1}, v_{z1}, \dots, v_{xN}, v_{yN}, v_{zN}\} = \delta \mathbf{e}_1$ , where  $\mathbf{e}_1$  is the eigenvector corresponding to  $\omega_1$  and  $\delta = \sqrt{2NK/m}$ , and run MD simulations at constant total energy for a given time  $t = \omega_1 \bar{t} / 2\pi$ . (The eigenvectors are normalized such that  $\mathbf{e}_i \cdot \mathbf{e}_j = \delta_{ij}$ , where  $\delta_{ij}$  is the Kronecker delta and  $i, j = 1, \dots, 3N - 6$  are the indexes of the eigenvectors that correspond to the non-trivial eigenfrequencies.)

We track the atom positions and velocities over long time periods  $t > 2700$  during the MD simulations. We then divide the long time series into 20 time intervals with equal duration  $\delta t = 135$ . We characterize the vibrational response of the system using two methods. In the first, we determine the vibrational response using the time period from 0 to  $\delta t$ . For the second method, we quantify how the vibrational response varies in time following the initial perturbation using a fixed tape length  $\delta t$  for each time interval. (We show that our results do not depend strongly on tape length  $\delta t$  in Appendix A.)

For each time interval between  $t$  to  $t + \delta t$ , we calculate the Fourier transform of the velocity autocorrelation function to determine the density of vibrational modes

$D(\omega, t)$  [37]:

$$D(\omega, t) = \int_0^{\delta t} \langle \mathbf{v}(t_0 + \tau) \cdot \mathbf{v}(t_0) \rangle_t e^{i\omega\tau} d\tau, \quad (1)$$

where  $\omega$  is the angular frequency and  $\langle \cdot \rangle_t$  indicates an

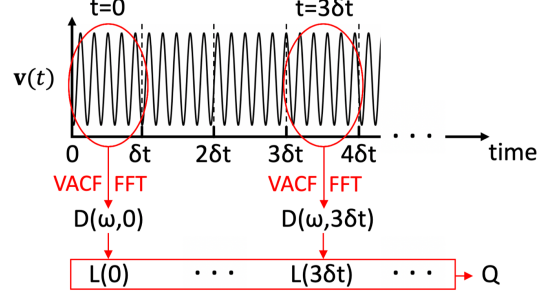


Figure 2: Schematic diagram that illustrates the method we use to calculate the loss  $L$  and quality factor  $Q$  of model metallic glass resonators. We track the velocities  $\mathbf{v}$  of the atoms in the resonator over a long time period. The time series is broken up into 20 time intervals with equal duration  $\delta t$ . We calculate the velocity auto-correlation function (VACF) for each time interval, and fast Fourier transform (FFT) it to measure the density of vibrational modes  $D(\omega, t)$  and loss  $L(t)$  for each time interval  $t$ . Using Eq. 3, we can calculate the quality factor  $Q$  from  $L(t)$ .

average over all atoms and time origins  $t_0$  between  $t$  and  $t + \delta t$ . See Fig. 2 for a summary of this approach.

For each time interval, we also determine the fraction of the kinetic energy that has transferred from the fundamental mode (with frequency  $\omega_1$ ) to other frequencies by defining the loss,

$$L(t) = 1 - \frac{\int_{\omega_1 - \Delta\omega}^{\omega_1 + \Delta\omega} D(\omega, t) d\omega}{\int_0^\infty D(\omega, t) d\omega}. \quad (2)$$

where  $\Delta\omega = (\omega_2 - \omega_1)/2$ . (See Fig. 3 (b).) By determining the loss  $L(t)$  over consecutive time intervals, we can calculate the quality factor

$$Q = \omega_1 \left( \frac{dL(t)}{dt} \right)^{-1}. \quad (3)$$

Note that the results do not depend strongly on the magnitude of  $\Delta\omega$  as long as it brackets  $\omega_1$ .

To track the atomic displacements during vibration, we will also calculate the root-mean-square deviation (RMSD) between two configurations, e.g.  $\mathbf{R}(t_1)$  and  $\mathbf{R}(t_2)$  at different times  $t_1$  and  $t_2$ :

$$d(\mathbf{R}(t_1), \mathbf{R}(t_2)) = \sqrt{N^{-1} \sum_{i=1}^N (x_i(t_1) - x_i(t_2))^2 + (y_i(t_1) - y_i(t_2))^2 + (z_i(t_1) - z_i(t_2))^2}, \quad (4)$$

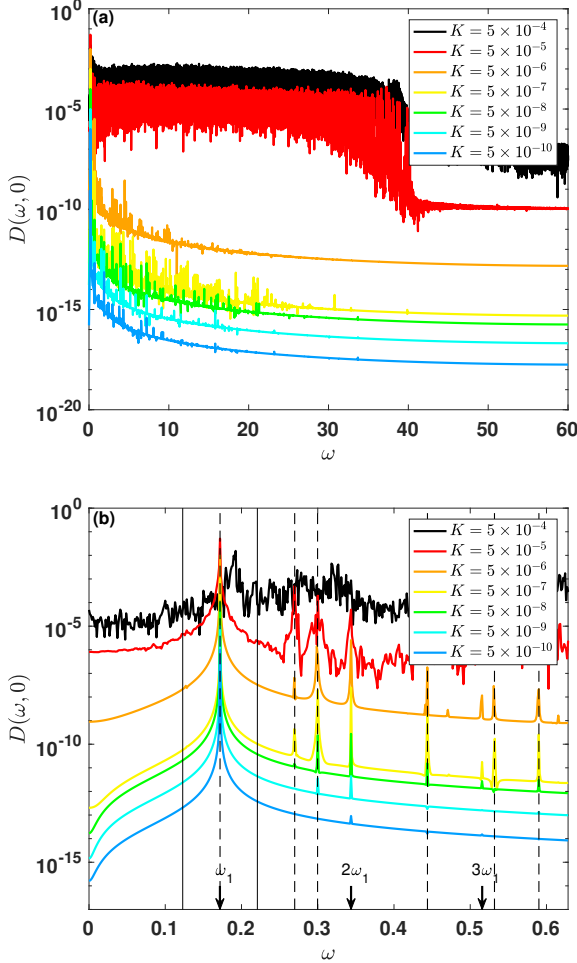


Figure 3: (a) The density of vibrational modes  $D(\omega, 0)$  for the time interval  $t = 0$  as a function of the kinetic energy per atom  $K$ . (b)  $D(\omega, 0)$  for the same systems in (a), but a close-up of the low frequency regime. The vertical dashed lines indicate the vibrational frequencies ( $\omega_1, \omega_2, \dots, \omega_{3N-6}$ ) calculated from the dynamical matrix. The arrows indicate integer multiples of the fundamental frequency  $\omega_1$  and the two vertical solid lines show the region of frequencies near  $\omega_1$  used in Eq. 2 to calculate the loss.

where the sum is over all atoms.

### III. RESULTS

The results are organized into three sections. In Sec. 3.1, we quantify the density of vibrational modes

$D(\omega, 0)$  and loss  $L(0)$  during the first time interval ( $t = 0$ ) as a function of the initial kinetic energy per atom  $K$ , and investigate the effects of atomic rearrangements on the vibrational response. We also study the dependence of  $D(\omega, t)$  and  $L(t)$  on the time interval  $t$  and calculate the quality factor  $Q$ . We identify three characteristic regimes for vibrational response as a function of  $K$ : the linear response regime, where there is no leakage of energy from the fundamental mode to others, the nonlinear regime, where energy leakage occurs at short times, but it stops at long times, and the strong loss regime where atomic rearrangements occur, causing large losses and small  $Q$ . In Sec. 3.2, we investigate how variations of the system size  $N$  and cooling rate  $R$  affect the frequency of atomic rearrangements, and thus the vibrational response. In Sec. 3.3, we calculate the loss in resonators made from polycrystalline and defected crystalline materials and compare it to resonators made from amorphous materials. We find that the losses generated from resonators with amorphous structure are comparable to that for crystalline resonators, and thus glassy materials may be promising for high- $Q$  resonator applications.

#### 3.1. Intrinsic dissipation: Nonlinearity and Atomic Rearrangements

We first focus on model metallic glass resonators with  $N = 2000$  generated using cooling rate  $R = 10^{-2}$ . In Fig. 3, we show the density of vibrational modes  $D(\omega, 0)$  after exciting the system along the fundamental mode as a function of the kinetic energy per atom over six orders of magnitude from  $K = 5 \times 10^{-10}$  to  $5 \times 10^{-4}$ . When  $K$  is small, most of the response remains in the fundamental mode,  $\omega_1$ , indicating that the system is in the linear response regime. As  $K$  increases, energy begins to leak to other modes of the dynamical matrix (indicated by the dashed vertical lines in Fig. 3 (b)), as well as harmonics of the fundamental mode (indicated by the arrows in Fig. 3 (b)). The leakage of energy from the fundamental mode is due to the nonlinearity of the Lennard Jones potential near the minimum and not due to the cutoff at  $r_c = 2.5\sigma_{ij}$  [38]. To test this, we also carried out studies of weakly nonlinear springs with  $r_c \rightarrow \infty$  and found similar results.

In Fig. 3, we show that there is a qualitative change in the vibrational response when  $K$  increases from  $5 \times 10^{-6}$  to  $5 \times 10^{-5}$ . At the higher value of  $K$ , the vibrational response is noisy and energy is redistributed over a much wider range of frequencies than at the lower value of  $K$ .

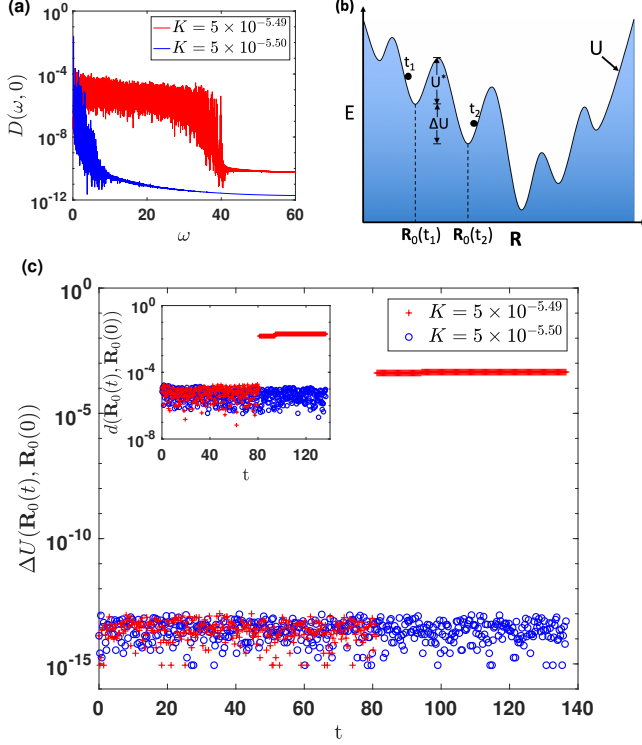


Figure 4: (a) Density of vibrational modes  $D(\omega, 0)$  for  $K = 5 \times 10^{-5.50}$  (blue) and  $5 \times 10^{-5.49}$  (red). (b) Schematic diagram of the energy landscape with axes, the total energy per atom  $E = U + K$  and atomic configuration  $\mathbf{R}$ . The configurations  $\mathbf{R}_0(t_1)$  and  $\mathbf{R}_0(t_2)$  represent the inherent structures (*i.e.*, the nearest local potential energy minima) of the vibrating system at times  $t_1$  and  $t_2$ , respectively.  $\Delta U$  is the difference in the potential energy per atom and  $U^*$  is the energy barrier between the configurations  $\mathbf{R}_0(t_1)$  and  $\mathbf{R}_0(t_2)$ . (c)  $\Delta U(\mathbf{R}_0(t), \mathbf{R}_0(0))$  between the inherent structures at times  $t$  and 0 for  $K = 5 \times 10^{-5.50}$  (blue circles) and  $5 \times 10^{-5.49}$  (red pluses). The inset shows the root-mean-square deviation (RMSD)  $d(\mathbf{R}_0(t), \mathbf{R}_0(0))$  between the inherent structures at times  $t$  and 0.

A more refined search shows that this qualitative change occurs in the kinetic energy interval  $5 \times 10^{-5.50} < K_r < 5 \times 10^{-5.49}$  as shown in Fig. 4 (a).

We now investigate the cause for the qualitative change in the vibrational response for  $K > K_r$ . To do this, for each fluctuating configuration  $\mathbf{R}(t)$ , we calculate the corresponding inherent structure, or the configuration of the nearest local potential minimum  $\mathbf{R}_0(t)$ , using conjugate gradient energy minimization. A schematic illustrating the potential energy landscape is shown in Fig. 4 (b). In Fig. 4 (c), we plot the difference in the potential energy per atom  $\Delta U(\mathbf{R}_0(t), \mathbf{R}_0(0)) = |U(\mathbf{R}_0(t)) - U(\mathbf{R}_0(0))|$  as a function of time for  $K < K_r$  and  $K > K_r$ . When  $K < K_r$ ,  $\Delta U \sim 10^{-14}$  for all times, indicating that the system remains in the basin of the inherent structure at  $t = 0$ . For  $K > K_r$ ,  $\Delta U$  jumps from  $\sim 10^{-14}$  to  $\sim 10^{-3}$  near  $t^* \sim 80$ , indicating that the system transitions from the basin of the inherent structure at  $t = 0$  to that of

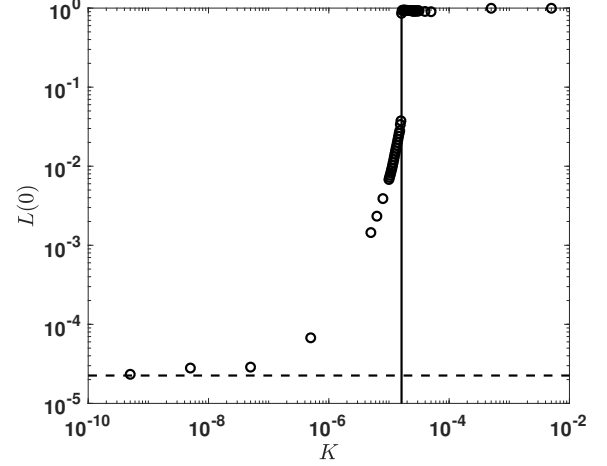


Figure 5: Loss  $L(0)$  (Eq. 2) for the first time interval  $t = 0$  versus the initial kinetic energy per atom  $K$ . The solid vertical line indicates  $K_r \approx 5 \times 10^{-5.49}$  at which the first atomic rearrangement occurs. The dashed horizontal line indicates the loss threshold  $L_l$  for a harmonic oscillator with a measurement time  $\delta t$  that deviates from an integer.

a different inherent structure at  $t^*$  following an atomic rearrangement. We also used Eq. 4 to calculate the root-mean-square deviation between the inherent structures  $\mathbf{R}_0(0)$  and  $\mathbf{R}_0(t)$  at times 0 and  $t$  during the vibrations. In the inset of Fig 4 (c), we show that  $\Delta U$  and  $d$  display similar behavior. For  $K < K_r$ ,  $d \sim 10^{-6}$  for all times. For  $K > K_r$ , near  $t^* \sim 80$ ,  $d$  jumps from  $\sim 10^{-6}$  to  $\sim 10^{-2}$  again indicating that an atomic rearrangement occurs at  $t^*$ . One can also see that subsequent rearrangements occur at later times, which are indicated by jumps in  $\Delta U$  and  $d$ . These results emphasize that atomic rearrangements induce significant redistribution of energy from the fundamental mode to other frequencies.

We quantify the leakage of energy from the fundamental mode to other frequencies over the first time interval  $t = 0$  by calculating the loss  $L(0)$  (defined in Eq. 2) as a function of  $K$  in Fig. 5. We calibrate the measurement of the loss by studying perfect cosine oscillations of the velocity of a single atom over a tape length of  $\delta t$ . Since in general  $\delta t$  is not an exact integer multiple of the oscillation period, the loss  $L_l \sim 10^{-4.5}$  we measured for a cosine wave is small, but nonzero. We find that the lower threshold for the loss  $L_l$  does not affect the results we present. In Fig. 5, we show that at small  $K$ ,  $L(0) \sim L_l$  and  $L(0)$  increases smoothly with increasing  $K$  until reaching 0.04 near  $K_r$ . At  $K_r$ , the loss jumps to  $L(0) \sim 1$ , indicating the onset of atomic rearrangements, and remains there for  $K > K_r$ .

In Fig. 5, we showed the loss for only the first time interval  $t = 0$ . We characterize the time-dependent loss in Fig. 6 (a). (We also include the variation of the density of states  $D(\omega, t)$  with time  $t$  in Appendix B.) We identify three distinct regimes. First, when  $K < K_{nl}$ , with  $K_{nl} \approx 1.15 \times 10^{-5}$  the loss  $L(t)$  is small and does not increase



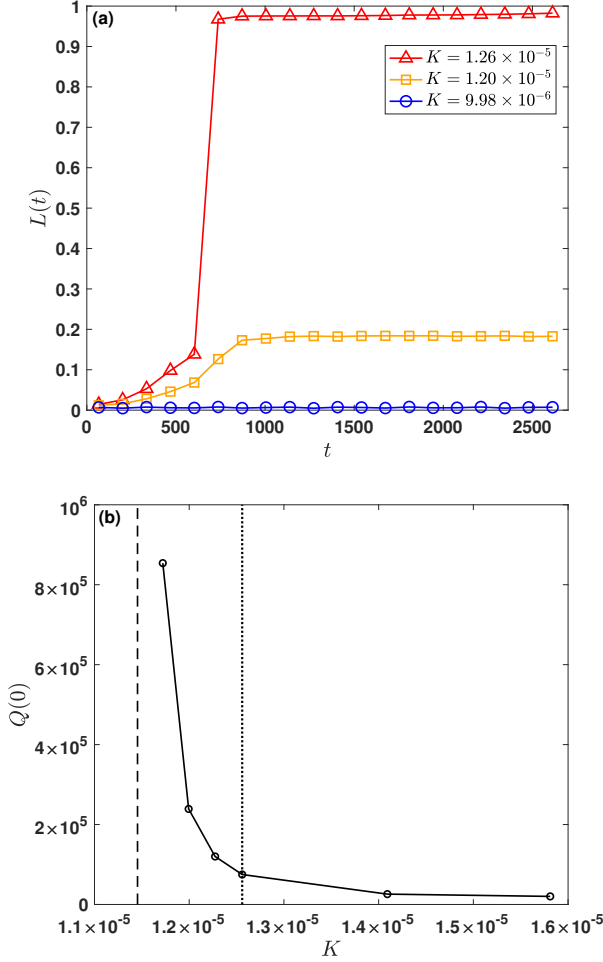


Figure 6: (a) Loss  $L(t)$  versus the time interval  $t$  for kinetic energy per atom  $K = 9.98 \times 10^{-6}$  (blue circles),  $1.20 \times 10^{-5}$  (orange squares), and  $1.26 \times 10^{-5}$  (red triangles). (b) Quality factor  $Q(0)$  for the first time interval  $t = 0$  as a function of  $K$ . The dashed vertical line indicates  $K_{nl} \approx 1.15 \times 10^{-5}$  at which  $Q(0) \rightarrow \infty$ . The vertical dotted line indicates  $K_r \approx 1.26 \times 10^{-5}$ , above which atomic rearrangements occur.

with  $t$ , and thus  $Q \rightarrow \infty$ . In the second regime, for intermediate  $K_{nl} < K < K_r$  (such as  $K = 1.20 \times 10^{-5}$  in Fig. 6 (a)),  $L(t)$  initially increases with  $t$  smoothly, generating a finite  $Q$ , but then  $L(t)$  reaches a plateau and  $Q \rightarrow \infty$  at long times. In the third regime, for  $K > K_r$  (such as  $K = 1.26 \times 10^{-5}$  in Fig. 6 (a)),  $L(t)$  increases with  $t$  smoothly (indicating finite  $Q$ ), until an atomic rearrangement event occurs and  $L(t)$  jumps to a large value  $L \sim 1$ .  $L(t)$  continues to increase after the first atomic rearrangement.

We evaluate  $Q(0)$  for the first time interval  $t = 0$  using Eq. 3, and show the results as a function of  $K$  in Fig 6 (b). We find that  $Q(0) \sim 2 \times 10^4$  for  $K \sim 1.5 \times 10^{-5}$  and  $Q(0)$  increases with decreasing  $K$ . For  $K \lesssim K_r$ ,  $Q$  begins to increase sharply, diverging as  $K \rightarrow K_{nl}$ , indicating the behavior for a perfect linear resonator for

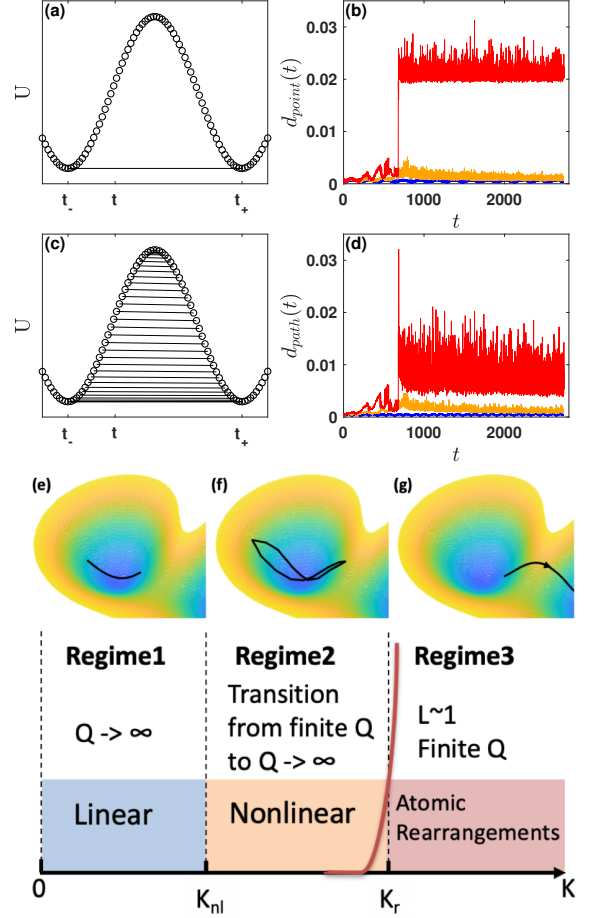


Figure 7: (a) and (c) Total potential energy per atom  $U$  as a function of time from 0 to  $n\delta t$ , where  $n = 20$ . The times  $t_-$  and  $t_+$  indicate successive times at which  $U$  is at a minimum during each half cycle. The horizontal solid line in (a), connecting the times  $t_-$  and  $t_+$ , indicates the times for each half cycle at which the RMSD,  $d_{\text{point}}(\mathbf{R}(t_-), \mathbf{R}(t_+))$ , is calculated in panel (b). In (b), we show  $d_{\text{point}}$  for  $K = 9.98 \times 10^{-6}$  in the regime  $K < K_{nl}$  (blue),  $K = 1.20 \times 10^{-5}$  in the regime  $K_{nl} < K < K_r$  (orange), and  $K = 1.26 \times 10^{-5}$  in the regime  $K > K_r$  (red). The horizontal solid lines in (c) indicate the times  $t_i$  and  $t_j = t_+ + t_- - t_i$  during each half cycle that are used to calculate the RMSD,  $d_{\text{path}} = \langle d(\mathbf{R}(t_i), \mathbf{R}(t_j)) \rangle_{t_i}$ , where the angle brackets indicate an average over the  $1/2\Delta t \sim 300$  uniformly spaced times  $t_i$ .  $d_{\text{path}}$  in panel (d) is shown for the same values of  $K$  as in (b). (e)-(g) Schematic diagram that shows the system trajectories (solid black lines) in the potential energy landscape (shaded contours from high (orange) to low (blue) energies) for the three regimes of oscillations (1:  $K < K_{nl}$ , 2:  $K_{nl} < K < K_r$ , and 3:  $K > K_r$ ). The red solid line indicates the probability of an atomic rearrangement versus  $K$ .

$K < K_{nl}$ . These results indicate that to design a high- $Q$  metallic glass resonator, one needs to fabricate a system with a large value for  $K_r$  and operate the resonator at  $K < K_r$ .

To understand the nature of oscillations in metallic glass resonators (e.g.  $U(t)$  in Fig. 7 (a) and (c)), we cal-

culate the point RMSD  $d_{\text{point}}(t)$  and path RMSD  $d_{\text{path}}(t)$  in Fig. 7 (b) and (d).  $d_{\text{point}}(t)$  quantifies the deviations in the configurations that are the closest to the potential energy minimum in each half cycle, and  $d_{\text{path}}(t)$  quantifies the deviations in the configurations at corresponding times before and after the turning point of the oscillation during each half cycle.

When  $K < K_{nl}$  (regime 1), the system is in the linear response regime, the path in configuration space followed by the resonator is nearly parabolic as shown in Fig. 7 (e), and both  $d_{\text{point}}$  and  $d_{\text{path}} \sim 0$ . When the system enters the nonlinear regime,  $K_{nl} < K < K_r$  (regime 2),  $d_{\text{point}}$  and  $d_{\text{path}}$  (as well as the loss  $L(t)$  in Fig. 6 (a)) increase with  $t$  until  $t^* \approx 790$ . For  $t > t^*$ ,  $d_{\text{point}}$ ,  $d_{\text{path}}$ , and  $L(t)$  reach plateaus and then remain nearly constant in time. This behavior indicates that the resonator is undergoing *nonlinear* oscillations, in which the system does not retrace the same configurations above and below the turning point for each half cycle, but the system is nearly reversible. (See Fig. 7 (f).) In the third regime  $K > K_r$ , the probability for an atomic rearrangement increases strongly. In this regime, the system can traverse the saddle points, enter the basins corresponding to new potential energy minima, and is thus microscopically irreversible. The three regimes describing resonator oscillations are summarized in Fig 7 (e)-(g).

### 3.2. Methods to increase $K_r$ and enhance $Q$

In Sec. 3.1, we showed that even single atomic rearrangements give rise to significant loss and finite values of  $Q$ . Thus, to generate high- $Q$  resonators, one must maximize  $\langle K_r \rangle \sim \langle U^* \rangle$ , yielding systems with large potential energy barriers. In this section, we describe studies of the ensemble-averaged  $\langle K_r \rangle$  versus system size  $N$  and cooling rate  $R$ , averaged over typically 20 independently generated initial conditions. For each  $R$  and  $N$ , we excite the resonator along the fundamental mode corresponding to the lowest eigenvalue of the dynamical matrix  $\omega_1$  and monitor the system during the first time interval  $t = 0$  as a function of  $K$ .

In Fig. 8 (a), we show that the ensemble-averaged kinetic energy per atom at which the first atomic rearrangement occurs,  $\langle K_r \rangle$ , decreases with increasing  $N$ . We find that  $\langle K_r \rangle \sim N^{-2k}$ , where  $k \approx 0.68$  for  $R = 10^{-2}$  and  $\approx 0.60$  for  $R = 10^{-5}$ .  $\langle K_r \rangle$  is smaller for rapidly compared to slowly cooled glasses, since  $\langle U^* \rangle$  decreases with increasing  $R$  [21, 39, 40]. These results emphasize that  $Q$  can be increased by making resonators smaller and preparing them using slower cooling rates. For example, experimental studies of Pt-based metallic glass micro-cantilevers have reported that the quality factor can be increased by more than a factor of 3 after annealing [9].

We can also compare the kinetic energy per atom  $\langle K_r \rangle$  required to induce the first atomic rearrangement in thermally vibrating systems to the characteristic shear strain  $\langle \gamma_r \rangle$  required to induce the first atomic rearrangement in

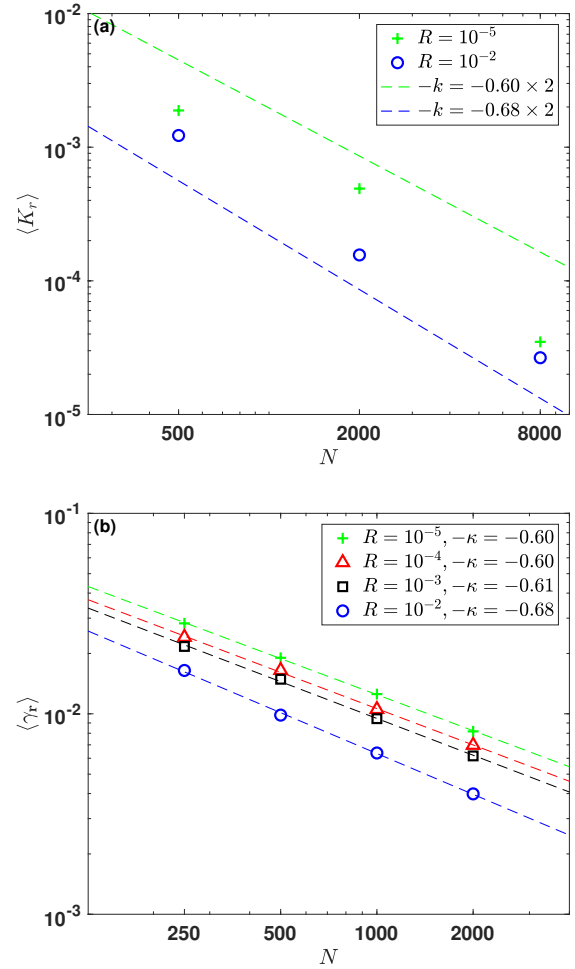


Figure 8: (a) The ensemble-averaged kinetic energy per atom  $\langle K_r \rangle$  above which the first atomic rearrangement occurs versus system size  $N$  for rapidly and slowly cooled glasses with  $R = 10^{-2}$  (blue circles) and  $10^{-5}$  (green pluses), respectively. In each case,  $\langle K_r \rangle$  is averaged over 20 independent samples. The slopes of the dashed lines are  $-k$ . (b) Ensemble-averaged pure shear strain  $\langle \gamma_r \rangle$  above which the first atomic rearrangement occurs during athermal quasistatic pure shear versus system size  $N$  for glasses prepared using  $R = 10^{-2}$  (blue circles),  $10^{-3}$  (black squares),  $10^{-4}$  (red triangles), and  $10^{-5}$  (green pluses).  $\langle \gamma_r \rangle$  is averaged over 500 independent samples. The negative  $\kappa$ -values give the slopes of the dashed lines.

systems driven by athermal quasistatic (AQS) shear. To calculate  $\langle \gamma_r \rangle$ , we confine  $N$  atoms interacting via the Kob-Andersen model to cubic boxes with periodic boundary conditions in the  $x$ -,  $y$ -, and  $z$ -directions. We cool the samples from temperature  $T_0$  to zero using a linear ramp over a range of cooling rates  $R$  from  $10^{-5}$  to  $10^{-2}$ . For each sample, we perform AQS pure shear at fixed volume  $V$ , i.e. at each strain step, we expand the box length and move all atoms affinely in the  $x$ -direction by a small strain increment  $\delta\gamma_x = \delta\gamma = 10^{-4}$  and compress the box length and move all atoms affinely in the  $y$ -direction by

the same strain increment  $\delta\gamma_y = -\delta\gamma$ . Following each strain step, we perform conjugate gradient energy minimization at fixed volume. To measure  $\langle\gamma_r\rangle$ , we employ the method we developed previously [19] to unambiguously determine whether an atomic rearrangement occurs with an accuracy on the order of numerical precision. As shown in Fig. 8 (b), we find that  $\langle\gamma_1\rangle \sim N^{-\kappa}$  also decreases with increasing  $N$ , where the system-size scaling exponent  $\kappa \sim 0.6$ -0.68 is again only weakly dependent on the cooling rate. These results for the system-size scaling exponents in athermal quasistatic shear are consistent with dimensional arguments that suggest  $\kappa \sim 2k$ , and thus athermal quasistatic shear can be used to understand the low temperature properties of glasses.

Using these results, we can estimate the strains below which resonators can operate in the linear response regime. For the slowest cooling rate  $R = 10^{-5}$ , we find that  $\log_{10}\langle\gamma_r\rangle \approx -2k\log_{10}N + \gamma_\infty$ , where  $2k \approx 0.60$ ,  $\gamma_\infty \approx 0.11$ ,  $N = \rho(l/D)^3$ , the number density  $\rho \approx 1.2$ ,  $D \approx 3.7 \text{ \AA}$  is a typical atomic diameter for  $\text{Ni}_{80}\text{P}_{20}$  metallic glasses [41] (which is the subject of the Kob-Andersen model), and  $l$  is a characteristic lengthscale of the resonator. We find that  $\langle\gamma_r\rangle \sim 5 \times 10^{-4}$  for a resonator with  $l \sim 20 \text{ nm}$ , whereas  $\langle\gamma_r\rangle \sim 3 \times 10^{-8}$  for a resonator with  $l \sim 5 \text{ }\mu\text{m}$  [42, 43]. Micron-scale metallic glass resonators have been fabricated as hemispherical shells [10] and as cantilevers [9]. In addition, strains in the range from  $10^{-7}$  to  $10^{-4}$  have been used in measurements of internal friction in metallic glass resonators [44]. Our results emphasize that nano-sized metallic glass resonators operating in the small strain regime (e.g.  $< 10^{-7}$ ) are promising high- $Q$  materials.

### 3.3. Comparison between crystalline and amorphous resonators

In Sec. 3.2, we showed that the characteristic kinetic energy per atom  $\langle K_r \rangle$  above which atomic rearrangements occur increases modestly with decreasing cooling rate. Further, we know that crystalline ordering increases with decreasing cooling rate. Does this imply that crystalline metals are higher- $Q$  materials compared to amorphous metals? In this section, we calculate  $\langle K_r \rangle$  for resonators made from single crystal, polycrystalline, and defected crystalline materials and compare these results to those for resonators made from homogeneously amorphous samples.

Crystalline metals often contain slip planes, dislocations, grain boundaries, and other defects, and the defect density typically increases with increasing cooling rate. To generate crystalline materials with defects in simulations, we will again use the Kob-Andersen model, but with monodisperse atoms,  $\epsilon_{AA} = \epsilon_{AB} = \epsilon_{BB} = 1.0$  and  $\sigma_{AA} = \sigma_{AB} = \sigma_{BB} = 1.0$ , to enhance crystallization. We will employ the same protocol as discussed in Sec. II to generate thin-bar resonators with  $N = 2000$  and aspect ratio  $L_x : L_y : L_z = 6 : 1 : 2$  over a range of cooling

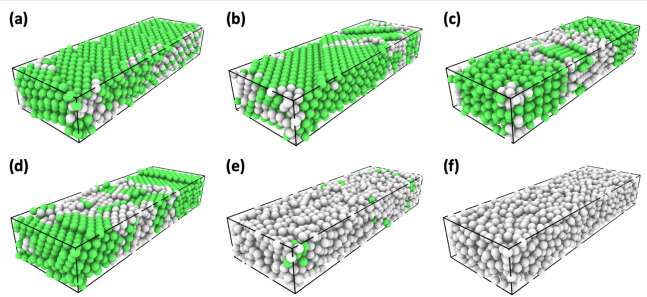


Figure 9: Snapshots of thin-bar-shaped resonators with  $N = 2000$  monodisperse atoms obtained using cooling rates (a)  $R = 1.2 \times 10^{-4}$ , (b)  $1.2 \times 10^{-3}$ , (c)  $3 \times 10^{-3}$ , (d)  $6 \times 10^{-3}$ , (e)  $1.2 \times 10^{-2}$ , and (f)  $1.2 \times 10^{-1}$  in periodic boundary conditions prior to applying the excitations. Atoms with crystalline (FCC or HCP) order are colored green, while amorphous atoms are colored gray.

rates from  $R = 10^{-4}$  to  $10^2$ . The method of excitation and measurement of the loss and  $K_r$  are also the same as described in Sec. II.

Snapshots of the zero-temperature thin-bar resonators generated using six different cooling rates are shown in Fig. 9 (with periodic boundary conditions and prior to adding excitations). We use the Common Neighbor Analysis (CNA) [45] to identify atoms that occur in crystalline (either face-centered cubic (FCC) or hexagonal close packed (HCP)) and amorphous environments in the thin bars. In Fig. 10 (a), we show that the ensemble-averaged fraction of crystalline atoms  $\langle f_X \rangle$  decreases with increasing  $R$ .  $\langle f_X \rangle$  is nearly 90% when  $R = 1.2 \times 10^{-4}$  and  $\langle f_X \rangle = 0$  for  $R = 1.2 \times 10^{-1}$ . Near the critical cooling rate  $R_c \approx 10^{-2.5}$ , the system contains a roughly equal mixture of atoms in crystalline and amorphous environments.

To quantify disorder in the thin-bar samples, we used the Dislocation Extraction Analysis (DXA) tool within the OVITO software library [46]. DXA allows us to measure the total dislocation length  $L_D$ , which gives the sum of the magnitudes of the Burgers vectors for each dislocation in the sample. For  $R \ll 1$ , we expect few defects, and thus  $\langle L_D \rangle \rightarrow 0$ . In Fig. 10 (b), for small  $R$ , we show that  $L_D$  increases with cooling rate  $R$  [7, 25]. When  $R > 3 \times 10^{-3}$ ,  $\langle L_D \rangle$  drops sharply since the thin-bar samples include mixtures of atoms with crystalline and amorphous environments.  $L_D \rightarrow 0$  when the sample becomes completely amorphous.

To determine the vibrational response, we excite the fundamental mode  $\omega_1$  for each sample, and measure  $\langle K_r \rangle$  as a function of  $R$ . The behavior for  $\langle K_r \rangle$  can be divided into four regimes. (See Fig. 10 (c).) First, at low cooling rates  $R \lesssim 3 \times 10^{-3}$  (regime I), the systems are mostly crystalline with sparse dislocations. In this regime, as  $R$  increases, more dislocations are formed and  $\langle L_D \rangle$  increases, which causes  $\langle K_r \rangle$  to decrease. In regime II, at intermediate cooling rates  $3 \times 10^{-3} \lesssim R \lesssim 1.2 \times 10^{-2}$ ,  $\langle f_X \rangle$  drops sharply and the thin bars contain mixtures of



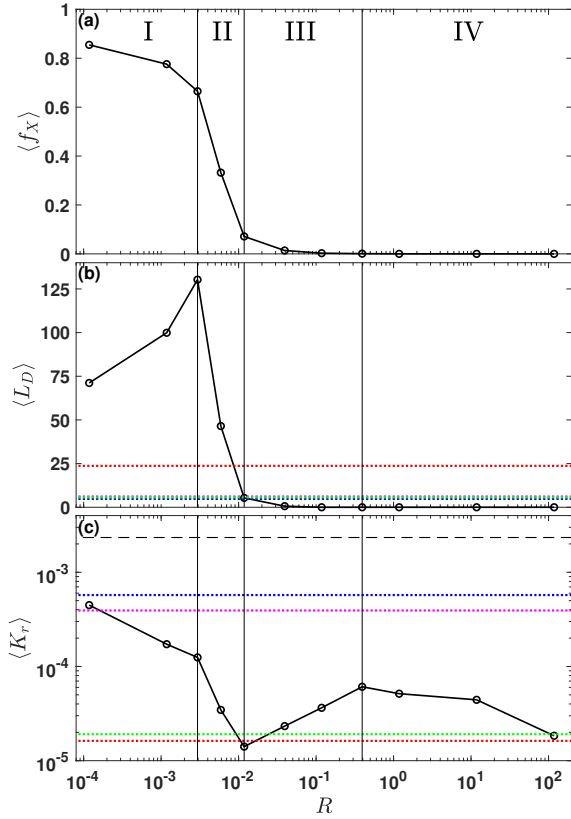


Figure 10: (a) Fraction of crystalline atoms  $\langle f_X \rangle$ , (b) total dislocation length  $\langle L_D \rangle$ , and (c) kinetic energy per atom  $\langle K_r \rangle$  above which atomic rearrangements occur as a function of cooling rate  $R$  for resonators made using the monodisperse Kob-Andersen model. The ensemble averages are obtained by averaging over at least 10 independent samples. The dotted horizontal lines in (b) and (c) show  $\langle L_D \rangle$  and  $\langle K_r \rangle$  for four nearly perfect, crystalline thin bars with specifically placed defects. For example, the red dotted lines represent the thin-bar sample in Fig. 11. The black dashed line in (c) shows  $\langle K_r \rangle$  for a thin bar with perfect FCC order. The solid vertical lines in panels (a)-(c) give approximate boundaries between the four regimes of vibrational response as a function of cooling rate  $R$ .

crystalline and amorphous atoms. The additional boundaries between amorphous and crystalline regions of the system causes a larger decrease in  $\langle K_r \rangle$  than at smaller  $R$ . In regime III,  $1.2 \times 10^{-2} \lesssim R \lesssim 3 \times 10^{-1}$ , the thin-bar resonators become homogeneously amorphous and metastable, causing  $\langle K_r \rangle$  to increase by a factor of  $\approx 4$ . At the high cooling rates  $R \gtrsim 3 \times 10^{-1}$  in regime IV,  $K_r$  will decrease modestly with increasing  $R$ . For the Kob-Andersen bidisperse mixture, we already showed in Fig. 8 (a) that  $\langle K_r \rangle$  decreases by a factor of  $\approx 3$  as  $R$  is increased over three orders of magnitude. This local maximum in  $\langle K_r \rangle(R)$  is interesting because it shows that there is a regime where amorphous resonators can have larger  $Q$ -values than partially crystalline resonators.

In addition to studying the vibrational response

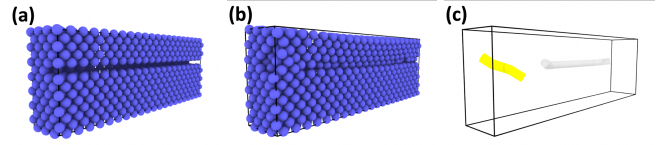


Figure 11: Snapshots of thin-bar crystalline resonators with a specifically placed defect. In (a), we delete a row of atoms from a resonator with perfect FCC order and perform energy minimization, which yields the thin-bar resonator in (b). (c) We identify two dislocations in the resonator in (b) colored yellow and gray.

of thin-bar resonators generated by cooling a high-temperature liquid into a solid, we also investigated the vibrational response of systems for which we started with perfect FCC crystalline thin bars and generated specifically placed defects. In particular, we generated four thin-bar samples that were initialized with perfect FCC order, and then we removed a slot with a width of one atom, depth of two atoms, and varying lengths along different directions in the sample. An example is shown in Fig. 11. We display  $\langle L_D \rangle$  and  $\langle K_r \rangle$  for these four systems in Fig. 10 (b) and (c). These samples possess a range of  $\langle K_r \rangle$ : some values are larger than that of the rapidly cooled glass ( $R = 1.2 \times 10^{-1}$ ), while others are not. These results show that amorphous resonators can possess values of  $\langle K_r \rangle$  (and thus  $Q$ ) that are comparable to those for crystalline samples. For example, the thin-bar resonator corresponding to the green dotted horizontal line in Fig. 10 (c) possesses a smaller  $\langle K_r \rangle$  than that of the rapidly cooled glass, with a dislocation density  $\langle L_D \rangle/V \approx 2 \times 10^{16} \text{ m}^{-2}$ , which is similar to the value for crystalline metals with strong dislocations [47]. Since metallic glasses do not need to be annealed, can be molded into complex shapes, possess unique magnetic and biocompatibility properties [13–15, 48, 49], and can possess comparable quality factors to crystalline metals [9], metallic glasses are promising materials for high- $Q$  applications.

#### IV. CONCLUSION

In this article, we employ molecular dynamics simulations of model metallic glass resonators undergoing vibrations to quantify the intrinsic dissipation and loss mechanisms caused by thermal fluctuations and atomic rearrangements. Using thin-bar resonators generated over a wide range of cooling rates, we excite the fundamental mode corresponding to the lowest eigenfrequency  $\omega_1$  of the dynamical matrix as a function of the kinetic energy per atom  $K$ . We find three regimes of vibration. In the linear response regime,  $K < K_{nl}$ , most of the energy of the vibrations remains in the fundamental mode, the loss is small, and  $Q \rightarrow \infty$  (since we do not consider coupling of the resonator to the environment). For  $K_{nl} < K < K_r$ , energy can leak from the fundamental

mode to others at short times, but at sufficiently long times the leakage of energy to other frequencies stops, and thus  $Q \rightarrow \infty$  at long times. For  $K > K_r$ , one or more atomic rearrangements occur. In this regime, energy in the fundamental mode is completely redistributed to a large set of other frequencies, the loss is large, and  $Q$  is finite. Thus, we show that  $K_r$  determines the quality factor.

We find that  $\langle K_r \rangle$  decreases as a power-law  $N^{-k}$  with increasing system size  $N$ , where  $k \approx 1.3$  decreases only modestly with decreasing  $R$ . We find similar results for the critical shear strain  $\langle K_r \rangle \sim \langle \gamma_r \rangle^2$  using athermal quasistatic shear deformation, where  $\langle \gamma_r \rangle$  is the characteristic strain above which atomic rearrangements begin to occur. Using these results, we estimate that  $\langle \gamma_r \rangle \sim 10^{-8}$  for micron-sized resonators, and thus large  $Q$ -values can be obtained when these resonators are operated at  $\gamma < \gamma_r$ . We also measured  $\langle K_r \rangle$  in thin-bar resonators with crystalline order and compared the vibrational response to that in amorphous resonators. We find that  $\langle K_r \rangle$  is similar for amorphous resonators and those with significant crystalline order. In light of the fact that metallic glasses can be thermoplastically formed into complex shapes, possess unique magnetic and biocompatibility properties, and can achieve  $Q$ -values that are comparable to those for crystalline structures, metallic glasses are promising materials for micro- and nano-resonators.

Our results raise a number of interesting future directions. For example, we can investigate methods that involve mechanical deformation, not slower cooling rates or annealing methods, to increase  $\langle K_r \rangle$  and move the sample to regions of configuration space with higher energy barriers between inherent structures. One possible approach is to apply athermal cyclic simple or pure shear deformation to samples that have been prepared using fast cooling rates. Recent studies have found that there is a finite critical strain amplitude for cyclic shear that marks the limit between reversible and irreversible atomic rearrangements in the large-system limit [50–52]. Does this imply that cyclic shear training can find zero-temperature configurations for which  $\langle K_r \rangle$  remains finite in the large-system limit? In addition, we can explore how the type of cyclic driving affects  $\langle K_r \rangle$  and whether configurations can be trained in multiple directions simultaneously to increase  $\langle K_r \rangle$ . Another future direction involves studies of the loss and quality factor when the resonator has clamped instead of free boundary conditions and when it is driven over a range of frequencies, not only the fundamental mode.

### Acknowledgments

The authors acknowledge support from NSF MRSEC Grant No. DMR-1119826 (M. F. and C.O.) and NSF Grant Nos. CMMI-1462439 (M. F. and C.O.) and CMMI-1463455 (M.S.). This work was supported by the

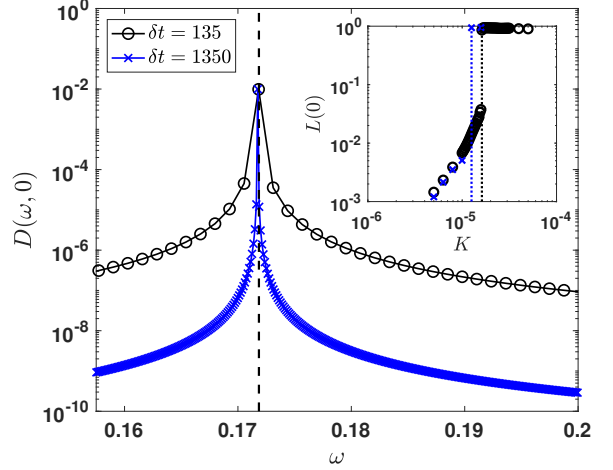


Figure 12: The low-frequency regime for the density of vibrational modes  $D(\omega, 0)$  near the fundamental frequency  $\omega_1 \approx 0.172$  (vertical dashed line) calculated using time series with two different total lengths,  $\delta t = 135$  (black circles) and  $1350$  (blue crosses), at  $K = 5 \times 10^{-6}$  in the linear response regime. In the inset, we show the loss  $L(0)$  versus  $K$  for the same time series in the main panel. The characteristic kinetic energy per atom above which an atomic rearrangement occurs are indicated:  $K_r = 1.62 \times 10^{-6}$  (black dotted line) for  $\delta t = 135$  and  $K_r = 1.26 \times 10^{-6}$  (blue dotted line) for  $\delta t = 1350$ .

High Performance Computing facilities operated by, and the staff of, the Yale Center for Research Computing.

### Appendix A: Length of time series

In the main text, we used a total run length of  $\delta t = 135$  to calculate the density of vibrational modes and loss for the first time interval  $t = 0$  in Figs. 3 and 5 (as well as all other time intervals). In this Appendix, we show results for  $D(\omega, 0)$  when  $\delta t$  is increased by a factor of 10 (keeping the sampling rate fixed). In Fig. 12, for  $K < K_r$  in the linear response regime, we show that the peak value of  $D(\omega_1, 0)$  is unchanged for  $\delta t = 135$  and  $1350$ , and thus  $L(0)$  is nearly the same for the two values of  $\delta t$ . We know that the probability for an atomic rearrangement increases with time  $\delta t$  at fixed  $K$ . Thus, in the inset to Fig. 12, we show that the loss  $L(0)$  undergoes a discontinuous jump for  $\delta t = 1350$  at a smaller  $K$  than that for  $\delta t = 135$ . We find that  $K_r \approx 1.62 \times 10^{-5}$  for  $\delta t = 135$  and  $\approx 1.26 \times 10^{-5}$  for  $\delta t = 1350$ . Thus, the precise value of  $K_r$  depends on  $\delta t$ , but all of the results are qualitatively the same for different choices of  $\delta t$ .

### Appendix B: Time-dependent density of vibrational modes

For the calculations of the density of vibrational modes and loss in the main text, we divided a long time series

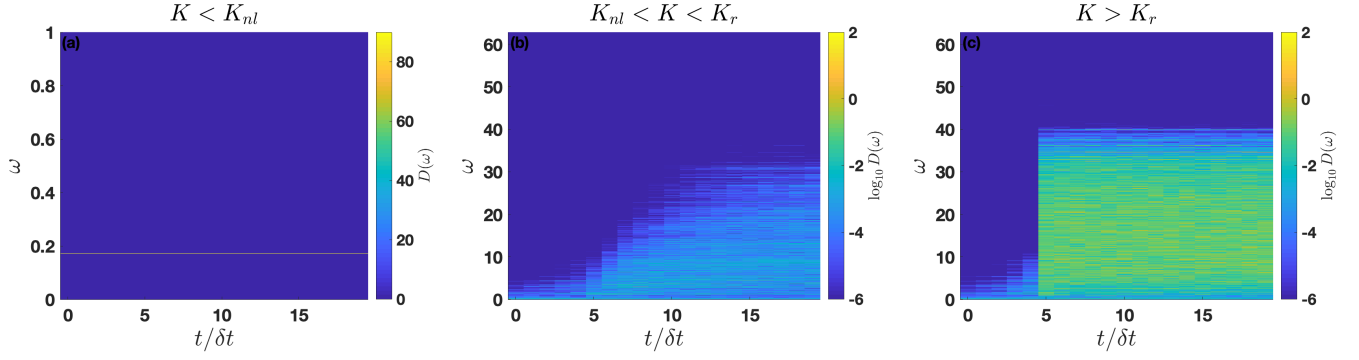


Figure 13: The density of vibrational modes  $D(\omega, t)$  versus time  $t/\delta t$  in the three regimes for the kinetic energy per atom, (a)  $K < K_{nl}$ , (b)  $K_{nl} < K < K_r$ , and (c)  $K > K_r$ , for a  $N = 2000$  thin-bar resonator with amorphous structure. The color scale from yellow to dark blue give decreasing values of  $D(\omega, t)$  in panel (a), and  $\log_{10} D(\omega, t)$  in panels (b) and (c).

following the excitation of the resonator along the fundamental mode into 20 time intervals of equal length  $\delta t$ . We showed the density of vibrational modes  $D(\omega, 0)$  for the first time interval (i.e. considering times from 0 to  $\delta t$ ) in Fig. 3. In this Appendix, we calculate  $D(\omega, t)$  for all 20 time intervals. We show  $D(\omega, t)$  for  $K$  values in the three regimes,  $K < K_{nl}$ ,  $K_{nl} < K < K_r$ , and  $K > K_r$ , which match those used in Fig. 6 (a). For  $K < K_{nl}$ , there

is minimal leakage of energy from the fundamental mode  $\omega_1 = 0.172$  and  $Q \rightarrow \infty$ . In the regime  $K_{nl} < K < K_r$ , energy leaks from the fundamental mode at short times, but it stops for  $t/\delta t \gtrsim 12$ , and the system vibrates nonlinearly with finite loss, finite  $Q$  for  $t/\delta t \lesssim 12$  and  $Q \rightarrow \infty$  for  $t/\delta t \gtrsim 12$ . For  $K > K_r$ , strong energy leakage occurs due to an atomic rearrangement at  $t/\delta t \approx 5$ .

- 
- [1] B. Arash, J.-W. Jiang, and T. Rabczuk, *Applied Physics Reviews* **2**, 021301 (2015).
  - [2] E. I. Green, *American Scientist* **43**, 584 (1955).
  - [3] M. E. Tobar, J. Krupka, J. G. Hartnett, E. N. Ivanov, and R. A. Woode, *IEEE Transactions on Ultrasonics, Ferroelectrics, and Frequency Control* **45**, 830 (1998).
  - [4] A. K. Huttel, G. A. Steele, B. Witkamp, M. Poot, L. P. Kouwenhoven, and H. S. van der Zant, *Nano Letters* **9**, 2547 (2009).
  - [5] H. Jiang, M.-F. Yu, B. Liu, and Y. Huang, *Physical Review Letters* **93**, 185501 (2004).
  - [6] P. Ovartchaiyapong, L. Pascal, B. Myers, P. Lauria, and A. Bleszynski Jayich, *Applied Physics Letters* **101**, 163505 (2012).
  - [7] M. S. Blanter, I. S. Golovin, H. Neuhauser, and H. Sinning, *Internal friction in metallic materials* (Springer, 2007).
  - [8] V. Khonik and L. Spivak, *Acta Materialia* **44**, 367 (1996).
  - [9] M. Kanik, P. Bordeenithikasem, G. Kumar, E. Kinser, and J. Schroers, *Appl. Phys. Lett.* **105**, 131911 (2014).
  - [10] M. Kanik, P. Bordeenithikasem, D. Kim, N. Selden, A. Desai, R. MCloskey, and J. Schroers, *Journal of Microelectromechanical Systems* **24**, 19 (2015).
  - [11] Y. Hiki, R. Tamura, and S. Takeuchi, *Materials Science and Engineering: A* **521**, 228 (2009).
  - [12] J. A. Bardt, G. R. Bourne, T. L. Schmitz, J. C. Ziegert, and W. G. Sawyer, *Journal of Materials Research* **22**, 339 (2007).
  - [13] J. Schroers, *Advanced Materials* **22**, 1566 (2010).
  - [14] G. Kumar, H. X. Tang, and J. Schroers, *Nature* **457**, 868 (2009).
  - [15] R. Li, Z. Chen, A. Datye, G. H. Simon, J. Ketkaew, E. Kinser, Z. Liu, C. Zhou, O. E. Dagdeviren, S. Sohn, et al., *Communications Physics* **1**, 75 (2018).
  - [16] M. A. Perez and A. M. Shkel, *IEEE Sensors Journal* **7**, 1653 (2007).
  - [17] A. M. Shkel, in *2006 IEEE/ION Position, Location, and Navigation Symposium* (IEEE, 2006), pp. 586–593.
  - [18] M. L. Falk and J. S. Langer, *Physical Review E* **57**, 7192 (1998).
  - [19] M. Fan, M. Wang, K. Zhang, Y. Liu, J. Schroers, M. D. Shattuck, and C. S. O'Hern, *Physical Review E* **95**, 022611 (2017).
  - [20] H. B. Yu, X. Shen, Z. Wang, L. Gu, W. H. Wang, and H. Y. Bai, *Physical Review Letters* **108**, 015504 (2012).
  - [21] M. Fan, K. Zhang, J. Schroers, M. D. Shattuck, and C. S. O'Hern, *Physical Review E* **96**, 032602 (2017).
  - [22] J. Zemp, M. Celino, B. Schönfeld, and J. F. Löffler, *Physical Review Letters* **115**, 165501 (2015).
  - [23] J. Ketkaew, W. Chen, H. Wang, A. Datye, M. Fan, G. Pereira, U. D. Schwarz, Z. Liu, R. Yamada, W. Dmowski, et al., *Nature communications* **9** (2018).
  - [24] C. Zener, *Physical Review* **52**, 230 (1937).
  - [25] A. S. Nowick, *Anelastic relaxation in crystalline solids*, vol. 1 (Elsevier, 2012).
  - [26] M. Barmatz and H. Chen, *Physical Review B* **9**, 4073 (1974).
  - [27] Y. Hiki, M. Tanahashi, and S. Takeuchi, *Journal of Non-Crystalline Solids* **354**, 994 (2008).
  - [28] H.-R. Sinning and F. Haeßner, *Zeitschrift für Physikalische Chemie* **156**, 115 (1988).
  - [29] K. Samwer, R. Rambousky, and M. Moske, in *Materials Science Forum* (Trans Tech Publ, 1995), vol. 179, pp. 761–768.

- [30] F. Spaepen, *Acta Metallurgica* **25**, 407 (1977).
- [31] J. Gilman, *Journal of Applied Physics* **44**, 675 (1973).
- [32] P. W. Anderson, B. Halperin, and C. M. Varma, *Philosophical Magazine* **25**, 1 (1972).
- [33] W. Phillips, *Journal of Low Temperature Physics* **7**, 351 (1972).
- [34] W. Kob and H. C. Andersen, *Physical Review E* **51**, 4626 (1995).
- [35] J. Wittmer, H. Xu, P. Políńska, F. Weysser, and J. Baschnagel, *Journal of Chemical Physics* **138**, 12A533 (2013).
- [36] A. Tanguy, J. Wittmer, F. Leonforte, and J.-L. Barrat, *Physical Review B* **66**, 174205 (2002).
- [37] T. Bertrand, C. F. Schreck, C. S. O'Hern, and M. D. Shattuck, *Physical Review E* **89**, 062203 (2014).
- [38] H. Mizuno, L. E. Silbert, M. Sperr, S. Mossa, and J.-L. Barrat, *Physical Review E* **93**, 043314 (2016).
- [39] H. Chen, H. Leamy, and M. Barmatz, *Journal of Non-Crystalline Solids* **5**, 444 (1971).
- [40] Y. Fan, T. Iwashita, and T. Egami, *Nature Communications* **5**, 5083 (2014).
- [41] H. Sheng, E. Ma, and M. J. Kramer, *Jom* **64**, 856 (2012).
- [42] P. Poncharal, Z. Wang, D. Ugarte, and W. A. De Heer, *Science* **283**, 1513 (1999).
- [43] S. Purcell, P. Vincent, C. Journet, and V. T. Binh, *Physical Review Letters* **89**, 276103 (2002).
- [44] V. Khonik, *Journal de Physique IV* **6**, C8 (1996).
- [45] J. D. Honeycutt and H. C. Andersen, *Journal of Physical Chemistry* **91**, 4950 (1987).
- [46] A. Stukowski, *Modelling and Simulation in Materials Science and Engineering* **18**, 015012 (2009).
- [47] E. Schafler, M. Zehetbauer, and T. Ungar, *Materials Science and Engineering: A* **319**, 220 (2001).
- [48] S. Li, S. Horikawa, M.-k. Park, Y. Chai, V. J. Vodyanoy, and B. A. Chin, *Intermetallics* **30**, 80 (2012).
- [49] J. Schroers, G. Kumar, T. M. Hodges, S. Chan, and T. R. Kyriakides, *Jom* **61**, 21 (2009).
- [50] I. Regev, J. Weber, C. Reichhardt, K. A. Dahmen, and T. Lookman, *Nature Communications* **6**, 8805 (2015).
- [51] D. Fiocco, G. Foffi, and S. Sastry, *Physical Review Letters* **112**, 025702 (2014).
- [52] P. Leishangthem, A. D. Parmar, and S. Sastry, *Nature Communications* **8** (2017).